CrystEngComm

Accepted Manuscript

ROYAL SOCIETY OF CHEMISTRY

www.rsc.org/crystengcomm

Facile synthesis of ultralong MnO_2 nanowires as high performance supercapacitor electrodes and photocatalysts with enhanced photocatalytic activities

Bosi Yin†, Siwen Zhang†, Yang Jiao, Yang Liu, Fengyu Qu, Xiang Wu*

Key Laboratory for Photonic and Electronic Bandgap Materials, Ministry of Education, Harbin Normal University, Harbin 150025, P. R. China

A simple hydrothermal route is developed for the synthesis of uniform α-MnO_2 nanowires using a controllable redox reaction in $MnCl_2$-$KMnO_4$ aqueous solution system. Electrochemical properties of the resultant products as the electrodes are investigated by the cyclic voltammetry, chronopotentiometry and electrochemical impedance test. The electrode can provide a specific capacitance of 180 $F \cdot g^{-1}$ at the current density of 1.0 $A \cdot g^{-1}$. After 2000 cycles, the specific capacitance maintains above 78%. Besides, the as-synthesized products are also used as the photocatalysts for the photocatalytic degradation of several dye molecules. The results show that almost complete degradation (~ 99%) of Congo red dye molecules in 30 min. Such ultralong MnO_2 nanowires might be expected to be potential applications in waste water treatment and energy storage.

To whom any correspondences should be addressed: E-mail: wuxiang@hrbnu.edu.cn

† These authors contributed equally to this work

1 Introduction

Nanostructured metal oxide semiconductors have attracted great attention in recent years due to their exceptional electronic, optical, electrochemical, and sensing properties.[1-7] Among various metal oxide nanostructures, manganese dioxide (MnO_2) has attracted intensive interest because of its low cost, environmental-compatibility and abundant availability.[8–10] MnO_2 can offer the opportunities in many applications related to Li-ion batteries,[11,12] supercapacitors, [13,14] gas sensors,[15] and catalysts.[16, 17] Significant efforts are being made to synthesize various MnO_2 nanostructures with high-yield and uniform sizes to improve their functionalities such as in eliminating toxic organic pollutants and clean energy devices. Zhang et al. have demonstrated the synthesis and efficient catalytic efficiency of one-dimensional β-MnO_2 nanorods as catalysts in the oxidation of methylene blue dye in the presence of H_2O_2.[18] Pal's group prepared novel hierarchical flower-like Ag-doped MnO_2 nanostructures using a facile wet chemical route.[19] Ge and his coworkers reported the degradation of azo dye acid red B on MnO_2 in the absence and presence of ultrasonic irradiation.[20] There are also many other reports about the electrochemical properties of MnO_2 nanostructures. Yuan et al. reported a novel and highly flexible solid-state supercapacitor based on a carbon nanoparticles/MnO_2 nanorods hybrid structures through a simple flame synthesis method and electrochemical deposition process.[21] Xie's group prepared ultrathin two-dimensional MnO_2/graphene hybrid nanostructures and investigated their supercapacitor performance.[22] Even though some progress have been made in synthesis and properties of MnO_2 nanostructures, it is still a huge challenge to seek

the facile preparation methods to obtain the desired MnO_2 architectures with various excellent performances.

Herein, we prepared ultralong MnO_2 nanowires by a facile hydrothermal route using a controllable redox reaction in $MnCl_2$-$KMnO_4$ aqueous solution system at mild temperature. Photocatalytic and electrochemical properties of the as-obtained product were investigated. The results showed that the as-obtained product exhibit an enhanced specific capacitance of 180 $F \cdot g^{-1}$ with high rate capability, and good cycling stability. The photocatalytic degradation experiments on Congo red, eosin red and methyl orange (MO) under UV irradiation showed that the as-synthesized ultralong MnO_2 nanowires possess high photodegradation efficiencies toward several organic dye molecules.

2 Experimental

All reagents in the experiments are of analytical grade and used without further purification. In a typical synthesis, 3 mmol $KMnO_4$ was dissolved into 30 mL deionized water and 5 mmol $MnCl_2 \cdot 4H_2O$ was dissolved into 10 mL deionized water in a 50 mL glass beaker with constantly stirring until the solution clear. The mixed solution was then put into a 100 ml sealed Teflon-lined autoclave, followed by a hydrothermal reaction at 120 ^oC for 10 h. After that, the autoclave was naturally cooled to room temperature and the obtained product was finally washed with deionized water and ethanol sequentially, and then dried at 60 ^oC for 12 h in air.

The crystalline structure of the as-obtained products were characterized using X-ray diffractometer (XRD, Rigaku Dmax-2600/pc, Cu K radiation, λ= 0.1542 nm,

40 KV, 150 mA). The detailed morphologies of the samples were characterized by scanning electron microscope (SEM, Hitachi-4800). The chemical and elemental compositions of the prepared products were checked by energy dispersive spectroscopy (EDS), attached with SEM, respectively. The microstructural characteristics were analyzed by Raman spectroscopy (LabRAM HR 800). The specific surface area of the prepared product was estimated using the Brunauer-Emmett-Teller (BET) equation based on the nitrogen adsorption isotherm obtained with a Belsorp-max. The pore size distribution was determined with the Barrett-Joyner-Halenda (BJH) method applied to the desorption branch of adsorption-desorption isotherm.

Electrochemical characteristics of the as-obtained products were studied on an CHI660 electrochemical work station (Chenhua, Shanghai) using cyclic voltammetry, chronopotentiometry and electrochemical impedance test by configuring the samples into a three electrodes cell, where the samples were used as the working electrode, Pt foil as the counter electrode and a saturated calomel electrode (SCE) as the reference electrode. The working electrodes were prepared as follows: the electrode of the obtained MnO_2 nanowires was prepared according to the following steps. A mixture containing 80 wt % MnO_2 products, 15 wt % acetylene black, and 5 wt % polytetrafluoroethylene (PTFE) was well mixed and dried under a vacuum at 120 ^oC for 5 h, the electrode area is 1 cm^2, and the loading density is about 1.0 $mg \cdot cm^{-2}$. The electrolyte used was 1.0 $mol \cdot L^{-1}$ Na_2SO_4 aqueous solution as an electrolyte at room temperature. The electrochemical properties and capacitive behavior of the

supercapacitor electrodes were evaluated by cyclic voltammetry (CV) and galvanostatic discharge. The specific capacitance, C ($F \cdot g^{-1}$), of the electrode material was calculated from the galvanostatic discharge according to the following equation

$$C = I\Delta t / (\Delta V m)$$

Where I is the discharge current (A), Δt is the discharge time (s), ΔV is the voltage change (V) excluding IR drop in the discharge process, and m is the mass of the active material (g). The electrochemical impedance spectroscopy (EIS) measurements were performed by applying an AC voltage with 5 mV amplitude in a frequency range from 0.01 Hz to 100 kHz.

The photocatalytic degradation experiments of three organic dyes (MO, eosin red and CR) were conducted by using the prepared MnO_2 product as the photocatalysts under UV light illumination. For the photocatalytic experiments, 0.1 g of MnO_2 nanowires were suspended in 200 mL of 40 $mg \cdot L^{-1}$ of organic dye aqueous solutions. The solutions were persistently stirred for 1 h in the dark to establish the adsorption-desorption equilibrium among MnO_2, organic dyes and water. Consequently, the resultant solutions were exposed to UV irradiation from a mercury lamp (500 W) at room temperature. The photocatalytic degradation of the organic dyes was estimated by measuring the absorbance of dye solution in the presence of photocatalyst exposed at different time. The degradation efficiencies of organic dyes were analyzed by monitoring the dye decolorization at the maximum absorption wavelength using UV-vis spectrophotometer (Shimazu UV-2550).

3 Results and Discussion

Morphology characterization of the as-prepared product are first conducted using SEM. Low magnification SEM image (Fig. 1a) shows large quantities of wire-like product. The nanowire possesses a length of tens of micrometers and an average diameter of 20 nm, as shown in Figure 1b. Further observation can be seen from low TEM image of the nanowire as shown Figure 1c, which suggesting the consistent result. Figure 1d is a HRTEM image taken from the α-MnO2 nanowire, revealing that the as-synthesized nanowire is single-crystalline, The observed interplanar spacing is 0.489 nm, which corresponds to the separation between (020) lattice planes of α-MnO_2. The inset in Figure 1d shows the corresponding SAED pattern taken from the nanowire. To further study the crystallinity and crystal phases of the as-obtained product, the prepared MnO_2 nanowires are analyzed by X-ray diffraction pattern. Figure 2a shows XRD pattern of the as-obtained product. All of the diffraction peaks are in accordance with the pure α-MnO_2 (JCPDS no. 44-0141). No peaks of other phases are detected, indicating high purity of the as-synthesized product. EDS spectrum (no shown) indicates that there is K element in the as-obtained product, which is because the material is derived from $KMnO_4$. The counter K^+ ion is inserted into the tunnel of MnO_2 nanostructures and evolved into stable α-phase structure. Raman spectrum of the as-prepared product is shown in Figure 2b. Three main peaks at 179, 574 and 637 cm^{-1} are observed, respectively. The band of 574 cm^{-1} is attributed to Mn-O lattice vibration in MnO_2. The band of 637 cm^{-1} is assigned to Mn_3O_4 formation during the spectrum acquisition because of local heating of the samples out of laser irradiation, which is consistent with the reported results.[23] In

addition, the observed Raman band of Mn_3O_4 is slightly shifted to the low frequency region compared to the reported data, which is due to the possible K^+ doping into α-MnO_2 nanowires.

MnO_2 microstructures consist of a series of allotropic forms on the basis of MnO_6 octahedra building blocks. In the designed $MnCl_2$-$KMnO_4$ redox system, both reducing agent and oxidizing agent are both from Mn compounds. The redox reaction comprises two half reactions:

$$Mn^{2+} + 2H_2O \rightarrow MnO_2 + 4H^+ + 2e^- \quad (E^o = 1.23V) \quad (1)$$

$$MnO_4^- + 4H^+ + 3e^- \rightarrow MnO_2 + 2H_2O \quad (E^o = 1.68V) \quad (2)$$

On the basis of the value of E^o, the standard Gibbs free energy change ΔG^o of redox reaction can be estimated to be -261 $kJ \cdot mol^{-1}$, ($\Delta G^o = -zFE$), demonstrating a very strong tendency for redox reaction to progress toward the right-hand side [24] It is reported that the crystallographic structure of MnO_2 can be controlled by K^+ cation, α-MnO_2 structure can be obtained by adding KCl.[25] KCl is also an important mineralizing agent during hydrothermal crystallization of inorganic compounds.[26] In our experiment, $KMnO_4$ can also provide K^+, which can thus favor formation of different crystallographic structures of MnO_2.[27] To more clearly describe its specific surface area and pore sizes, we used Brunauer-Emmett-Teller theory and Barrett-Joyner-Halenda (BJH) theory, which are presented in Figure 3. Quantitative calculation demonstrates that the as-prepared MnO_2 product possesses a BET surface area of 61.499 $m^2 \cdot g^{-1}$. The large value may be attributed to the small aperture character of the prepared material. The narrow size distribution of ~3.8 nm of the

prepared material could be originated from the gap between the adjacent small nanostructures. It can be determined that large BET surface area and small aperture of ultralong MnO_2 nanowire architecture can provide a shortened diffusion path for electrons and ions which can enhance the supercapacitor peformance. Besides, the photo-generated electrons and holes also recombine easily on the surface of the semiconductor. Therefore the structure of the products can get more reactive species, which lead to the photocatalytic efficiency being enhanced.

To further explore potential applications in the supercapacitor of the obtained product, the electrochemical performances of the as-synthesized MnO_2 nanowires as the integrated electrode were evaluated. CV curves of the working electrode collected at various scan rates ranging from 10 to 200 $mV \cdot s^{-1}$ are shown in Figure 4a. It shows that with the increase of the scan rate, the area enclosed by the CV curves increases, the redox current increased. The shapes of these curves are quasi-rectangular, indicating the ideal electrical double-layer capacitance behavior and fast charging/discharging process characteristic. Even at a high scan rate of 200 $mV \cdot s^{-1}$, the shapes of CV curves remain undistorted, implying low contact resistance in the supercapacitor. A galvanostatic discharging test was also performed with different current densities 1.0, 2.0, 3.0, 5.0 and 8.0 $A \cdot g^{-1}$, as shown in Figure 4b. The linear voltage versus time profiles and a quick I-V response suggest that MnO_2 nanowires are good electrode materials in supercapacitors. Electrochemical impedance spectroscopy (EIS) was applied to investigate the electrical conductivity and ion transfer of the supercapacitor cells. Figure 4c displays the Nyquist plots of MnO_2

product. The EIS data can be fitted by an equivalent circuit as shown inset in Figure 4c. First, the intercept on the real axis in high frequency range provides the equivalent series resistance (ESR) (Rs), which includes the inherent resistances of the electroactive material, the bulk resistance of electrolyte and the contact resistance at the interface between the electrolyte and electrode. Its range also corresponds to the charge transfer resistance caused by the Faradic reaction, which is correlated with the intercalation and deintercalation of ions. The charge transfer resistance (Rct), which results from diffusion of electrons, can be calculated from the diameter of the semicircle in the high frequency range. The Warburg resistance (Rw), which describes the diffusion of redox species in the electrolyte, can be reflected from the slope of the EIS curve in the low frequency range.[28] Its range corresponds to the diffusion-limited mechanism, which confirms that the main capacitive behaviour. Qc represents the constant phase element accounting for a double-layer capacitance. The intercept of the Nyquist curve on the real axis (Rs) demonstrates good conductivity and very low internal resistance of MnO_2 electrode. In addition, the charge-transfer resistance Rc_t, also called Faraday resitance, is a limiting factor for the specific power of the supercapacitor.[29] The calculated capacitances as a function of discharge current densities are plotted in Figure 4d. Impressively, MnO_2 electrode delivers special capacitance of 180, 128, 96, 90 and 72 $F \cdot g^{-1}$ at current densities of 1.0 $A \cdot g^{-1}$, 2.0 $A \cdot g^{-1}$, 3.0 $A \cdot g^{-1}$, 5.0 $A \cdot g^{-1}$ and 8.0 $A \cdot g^{-1}$, respectively. The enhanced electrochemical performance could be attributed to reduced diffusion path of ions, highly accessible surface area and increased electrical conductivity by ultralong MnO_2 nanowires

structure. Figure 4e demonstrates the cycling performance of the device up to 2000 cycles at the current density of 1.0 $A \cdot g^{-1}$. A specific capacitance of 180 $F \cdot g^{-1}$ and a good reversibility with cycling efficiency of 78% after 2,000 cycles are shown in inset in Figure 4e. As we can see in Figure 4f, when the current density increases to 8 $A \cdot g^{-1}$, the specific capacitance is 72 $F \cdot g^{-1}$, maintaining 40% of that at the current density of 1 $A \cdot g^{-1}$. This conclusion provides the opportunity for working under high current density.

To demonstrate the photocatalytic activities of the as-synthesized MnO_2 nanowires for the degradation of organic pollutants, we conducted photocatalytic degradation experiments of methyl orange (MO), eosin red and Congo red (CR). The initial concentration for all the organic dyes is 40 $mg \cdot L^{-1}$. Figure 5a shows the adsorption spectrum of MO dye over the prepared MnO_2 nanowires measured at different intervals of time. The characteristic absorption peak at 465 nm decreases gradually with the increasing of the illumination time. Obviously, MO is degraded about 94% when radiation time reaches 90 min. The adsorption spectrum of eosin red in aqueous solution under the same condition is shown in Figure 5b. It indicates that eosin red is degraded 96% after 35 min. Finally, further comparison was made to investigate the photocatalytic activity of MnO_2 products for the degradation of CR in aqueous solution. The intensity of characteristic adsorption peak (495 nm) of CR diminished gradually with extension of exposure time (Figure 5c), decomposing about 99% after 30 min of irradiation. The results suggest that the as-synthesized MnO_2 nanowires exhibited excellent photocatalytic activity toward MO, eosin red and CR.

Different degradation efficiencies for MO, eosin red and CR can be observed directly in Figure 5d. In order to illustrate for which dyes MnO_2 nanowires are highly selective, we take the same 30 min to compare degradation efficiency of different dyes according to Figures 5a-c. The changes of the organic pollutants concentration under ultraviolet irradiation can be calculated as follows:

$$I = C / C_0 \times 100\%$$

Where C_0 is the initial concentration of organic pollutants when ultraviolet light is turned on, while the real time concentration of organic pollutants under the ultraviolet light irradiation is expressed by C. Photocatalytic efficiency derived from the changes of organic dyes concentration can be represented by the relative ratio C/C_0. The order of degradation rate was MO (94%) < eosin red (96%) < CR (99%), as shown in Figure 5d. Obviously, ultralong MnO_2 nanowires possess the highest degradation efficiency to CR solution.

In general, during photocatalytic degradation of dye molecules, hydroxyl radicals (·OH) plays a main role.[30] Therefore, increasing the percentage of ·OH in the reaction system can immediately increase the photocatalytic efficiency. On the basis of the photocatalysis mechanism (Figure 6), the ·OH generated from the oxidization of H_2O by photo-generated holes (h^+) and the deoxidization of O_2 by photo-generated electrons (e^-) by UV irradiation.[31] Nevertheless, the photo-generated electrons and holes can recombine easily in the volume or on the surface of the semiconductor.[32] Hence, two ways can be tried to enhance the photocatalytic efficiency of MnO_2 nanowires. First, the decrease in the recombination of the photo-generated electrons

and holes allows them to take part in the photocatalytic reaction. Second, optimizing the morphology and structure of the products can get more reactive species, thus, the photocatalytic efficiency was enhanced. In our experiments, the remarkable photocatalytic activities of MnO_2 nanowires may be attributed to ultralong and mesoporous structure. This structure can provide more active sites to adsorb reactive species and O_2 and allow more effective transport for the reactant molecules to get to the active sites.

4 Conclusions

In summary, we synthesized ultralong MnO_2 nanowires by a simple one-step solution route in a controllable redox $MnCl_2$-$KMnO_4$ aqueous solution system. Such material with large BET surface area and the narrow size distribution gives ideal capacitor behavior and complete degradation of organic dye molecules. Electrochemical measurements show that the nanowires demonstrate many advantages in performance such as high specific capacitance, good charge-discharge stability, long-term cycling life, and low leakage current. It can be determined that the ultralong MnO_2 nanowire architecture provides a shortened diffusion path for electrons and ions. In addition, the as-synthesized MnO_2 nanowires also exhibit a remarkable photocatalytic activity for degradation of organic dyes.

Acknowledgement:

This work was supported by the Scientific Research Fund of Heilongjiang Provincial Education Department (12531179) and Program for Scientific and Technological Innovation Team Construction in Universities of Heilongjiang (No.

2011TD010).

References

1. Y. T. Han, X. Wu, Y. L. Ma, L. H. Gong, F. Y. Qu and H. J Fan, *CrystEngComm*, 2011, **13**, 3506.
2. Z. Song, S. A. Kulinich, J. Yan, Z. G. Li, J. P. He, C. X. Kan and H. B. Zeng, *Adv. Mater.*, 2013, **25**, 5677.
3. Y. Lei, F. Y. Qu and X. Wu, *Nano-Micro Lett.*, 2012, **4**, 45.
4. H. B. Zeng, G. T. Duan, Y. Li, S. K. Yang, X. X. Xu and W. P. Cai, *Adv. Funct. Mater.*, 2010, **20**, 561.
5. X. Zhang, H. H. Liu, S. Petnikota, S. Ramakrishna and H. J. Fan, *J. Mater. Chem. A,* 2014, **2**, 10835.
6. Y. Liu, Y. Jiao, Z. L. Zhang, F. Y. Qu, A. Umar and X. Wu, *ACS Appl. Mater. Interfaces*, 2014, **6**, 2986.
7. Z. L. Zhang, H. Y. Song, S. S. Zhang, J. Y. Zhang, W. Y. Bao, Q. Q. Zhao and X. Wu, *CrystEngComm*, 2014, **16**, 110.
8. Q. F. Wang, J. Xu, X. F. Wang, B. Liu, X. J. Hou, G. Yu, D. Chen and G. Z. Shen, *ChemElectroChem*, 2014, **1**, 559.
9. W. Y. Li, G. Li, J. Sun, R. Zou, K. Xu, Y. Sun, Z. Chen, J. Yang and J. Q. Hu, *Nanoscale*, 2013, **5**, 2901.
10. W. Xiao, D. Wang and X. W. Lou, *J. Phys. Chem. C*, 2010,**114**,1694.
11. R. C. Lee, Y. P. Lin, Y. T. Weng, H. A. Pan, J. F. Lee and N. L. Wu, *J. Power. Sources*, 2014, **253**, 373.

12. Y. Y. Li, Q. W. Zhang, J. L. Zhu, X. L. Wei and P. K. Shen, *J. Mater. Chem. A*, 2014**, 2,** 3163.

13. J. P. Liu, J. Jiang, C. W. Cheng, H. X. Li, J. X. Zhang, H. Gong and H. J. Fan, *Adv. Mater.*, 2011, **23**, 2076.

14. S. Chen, J. Zhu, X. Wu, Q. Han and X. Wang, *ACS Nano*, 2010, **4**, 2822.

15. K. Miyazaki, M. Hieda and T. Kato, *Ind. Eng. Chem. Res.*, 1997, **36**, 88.

16. F. Cheng, J. Shen, W. Ji, Z. Tao, J. Chen, *ACS Appl. Mater. Interfaces*, 2009, **1**, 460.

17. L. Espinal, S. L. Suib and J. F. Rusling, *J. Am. Chem. Soc*, 2004, **126**, 7676.

18. W. X. Zhang, Z. H. Yang, X. Wang, Y. C. Zhang, X. G. Wen and S. H. Yang, *Catal. Commun.*, 2006, **7**, 408.

19. S. Jana, S. Pande, A. K. Sinha, S. Sarkar, M. Pradhan, M. Basu, S. Saha and T. Pal, *J. Phys. Chem. C*, 2009, **113**, 1386.

20. J. T. Ge and J. H. Qu, *J. Hazardous Mater.*, 2003, **100**, 197.

21. L. Y. Yuan, X. H. Lu, X. Xiao, T. Zhai, J. J. Dai, F. C. Zhang, B. Hu, X. Wang, L. Gong, J. Chen, C. G. Hu, Y. X. Tong, J. Zhou and Z. L. Wang, *ACS. Nano*, 2012, **6**, 656.

22. L. L. Peng, X. Peng, B. R. Liu, C. Z. Wu, Y. Xie and G. H. Yu. *Nano Lett.*, 2013, **13**, 2151.

23. J. Luo, H. T. Zhu, H. M. Fan, J. K. Liang, H. L. Shi, G. H. Rao, J. B. Li, Z. M. Du and Z. X. Shen, *J. Phys. Chem. C*, 2008, **112**, 12594.

24. X. Wang and Y. Li, *J. Am. Chem. Soc.*, 2002, **124**, 2880.

25. X. Huang, D. Lv, H. Yue, A. Attia and Y. Yang, *Nanotechnology*, 2008, **19**, 225606.

26. F. Zhou, H. Zheng, X. Zhao, Q. Guo, X. Ni, T. Shen and C. Tang, *Nanotechnology*, 2005, **16**, 2072.

27. J. Wang, X. M. Fan, K. Tian, Z. W. Zhou and Y. Wang, *Appl. Surf. Sci.*, 2011, **257**, 7763.

28. R. B. Rakhi, W. Chen, D. Cha and H. N. Alshareef, *Nano Lett.*, 2012, **12**, 2559.

29. J. F. Zang, S. J. Bao, C. M. Li, H. J. Bian, X. Q. Cui, Q. L. Bao, C. Q. Sun, J. Guo and K. R. Lian, *J. Phys. Chem. C*, 2008, **112**, 14843.

30. J. Wang, X. M. Fan, K. Tian, Z. W. Zhou, Y. Wang, *Appl. Surf. Sci.*, 2011, **257**, 7763.

31. M. Kong, Y. Z. Li, X. Chen, T. T. Tian, P. F. Fang, F. Zheng, X. J. Zhao, *J. Am. Chem. Soc.*, 2011, **133**, 16414.

32. H. F. Cheng, B. B. Huang, Y. Dai, X. Y. Qin, X. Y. Zhang, *Langmuir*, 2010, **26**, 6618.

Figures caption

Fig.1 (a-b) SEM images of the as-synthesized MnO_2 nanowires at different magnification. (c) TEM image of the nanowires; (d) HRTEM image of the nanowire. The inset image is the SAED pattern.

Fig. 2 (a) XRD pattern of the as-synthesized MnO_2 product. (b) Raman spectrum of the as-synthesized products.

Fig.3 (a) Typical nitrogen adsorption-desorption isotherm and the inset is BJH pore size distribution plots of the prepared MnO_2 nanostructures.

Fig.4 (a) CV curves at scan rates between 10 and 200 $mV \cdot s^{-1}$. (b) charge-discharge curves at current densities ranged from 1.0 to 8.0 $A \cdot g^{-1}$. (c) EIS spectra of MnO_2 nanowires electrode. (d) Current density dependence of the specific capacitance. (e) Cycle life of MnO_2 electrode. The inset image is cycling performance at current density of 1.0 $A \cdot g^{-1}$. (f) Capacitance retention ratio as a function of discharge current densities.

Fig.5 Variations in adsorption spectra of organics dye solution in the presence of MnO_2 products irradiated by a UV lamp for different time: (a) MO, (b) eosin red, (c) CR, and (d) Photocatalytic degradation rate of MO, eosin red, and CR.

Fig.6 Photocatalytic schematic of the as-synthesized MnO_2 nanowires.

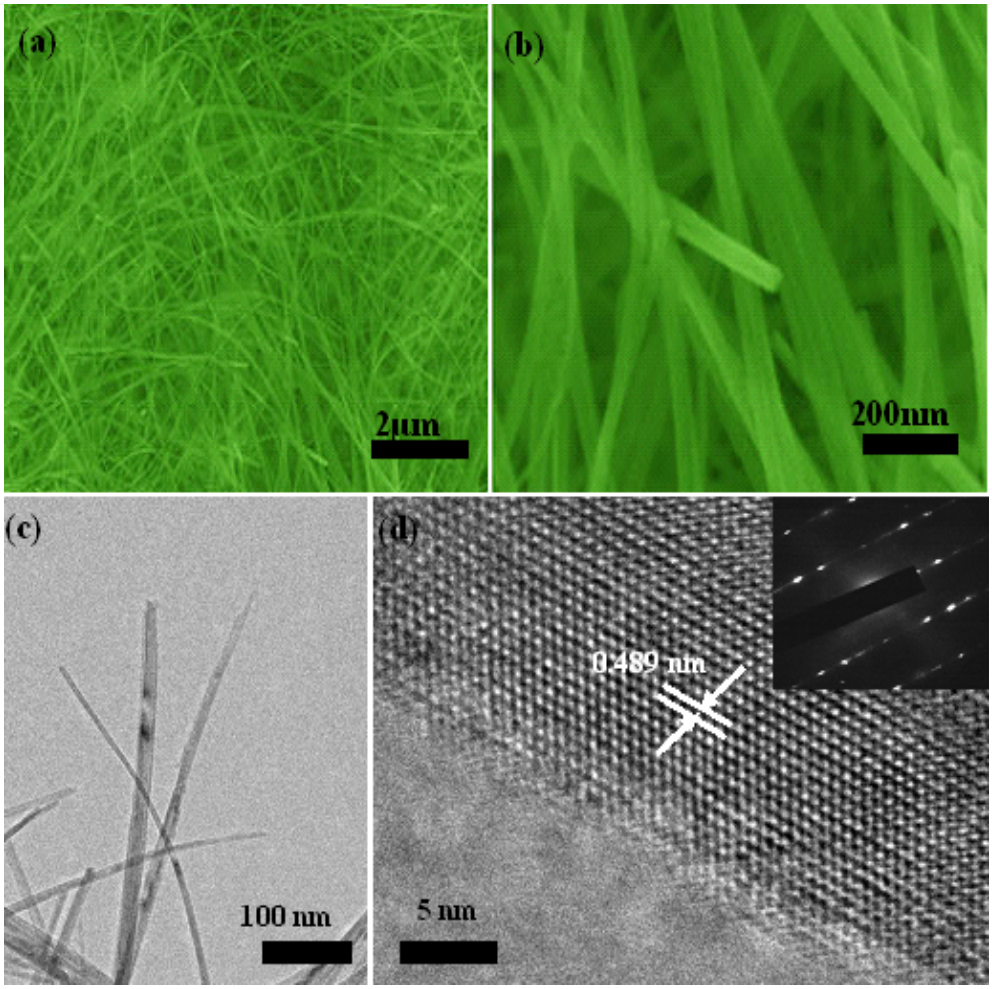

Fig. 1 Bosi Yin et al.

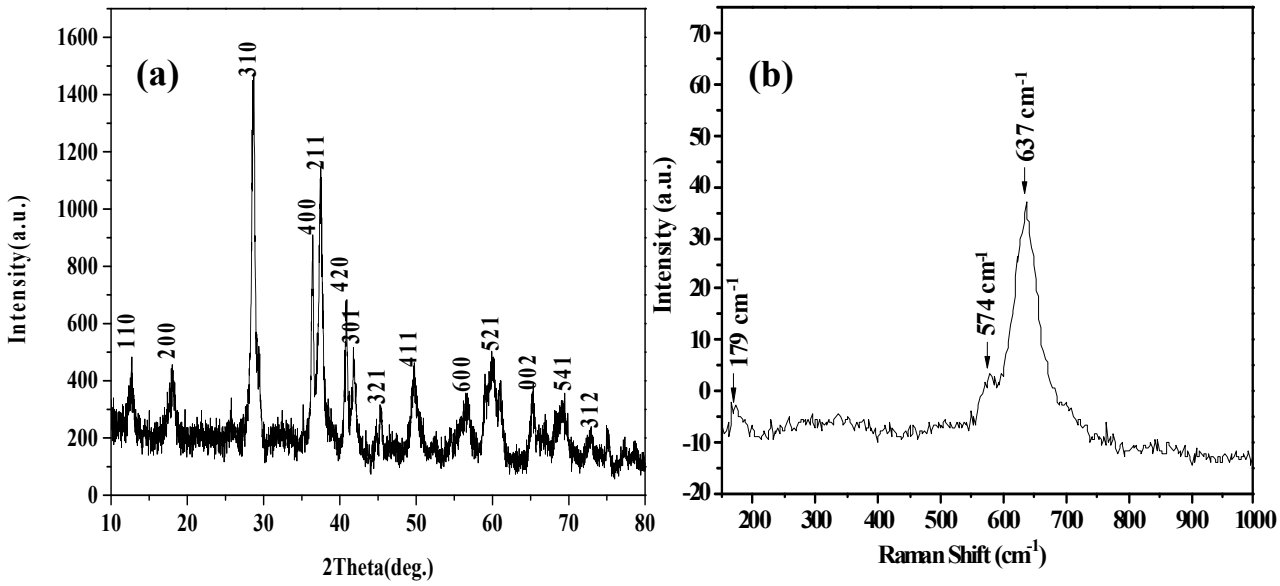

Fig. 2 Bosi Yin et al.

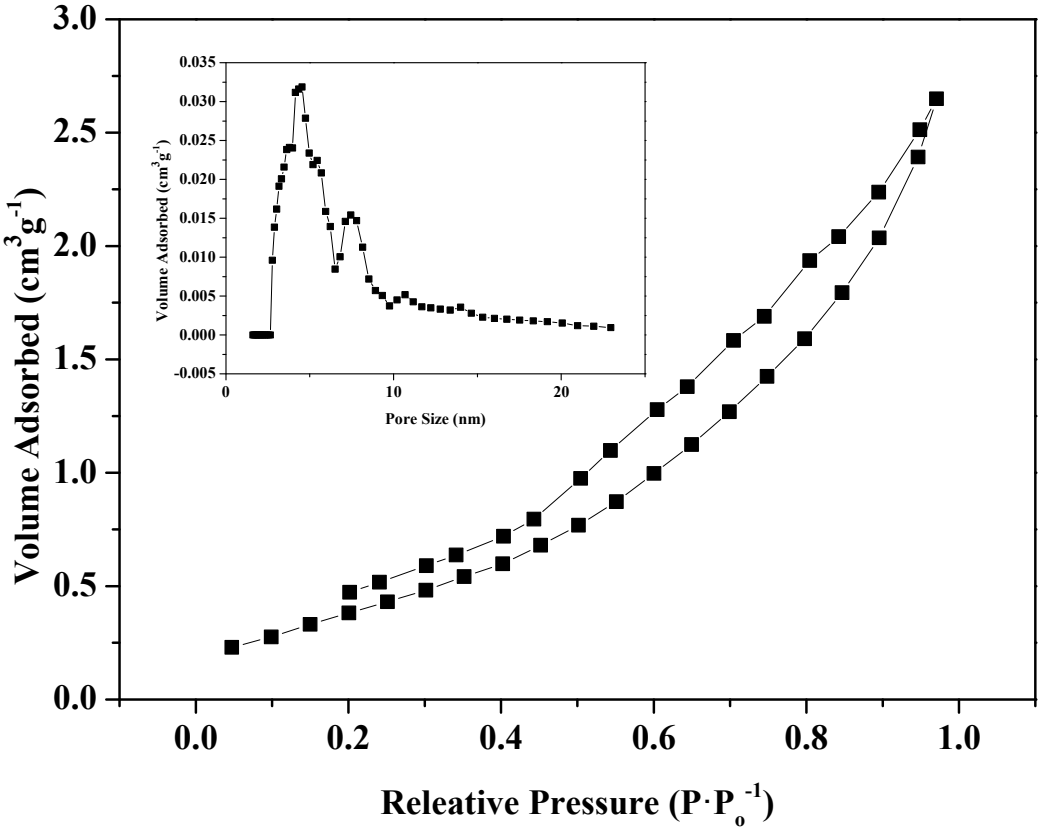

Fig. 3 Bosi Yin et al.

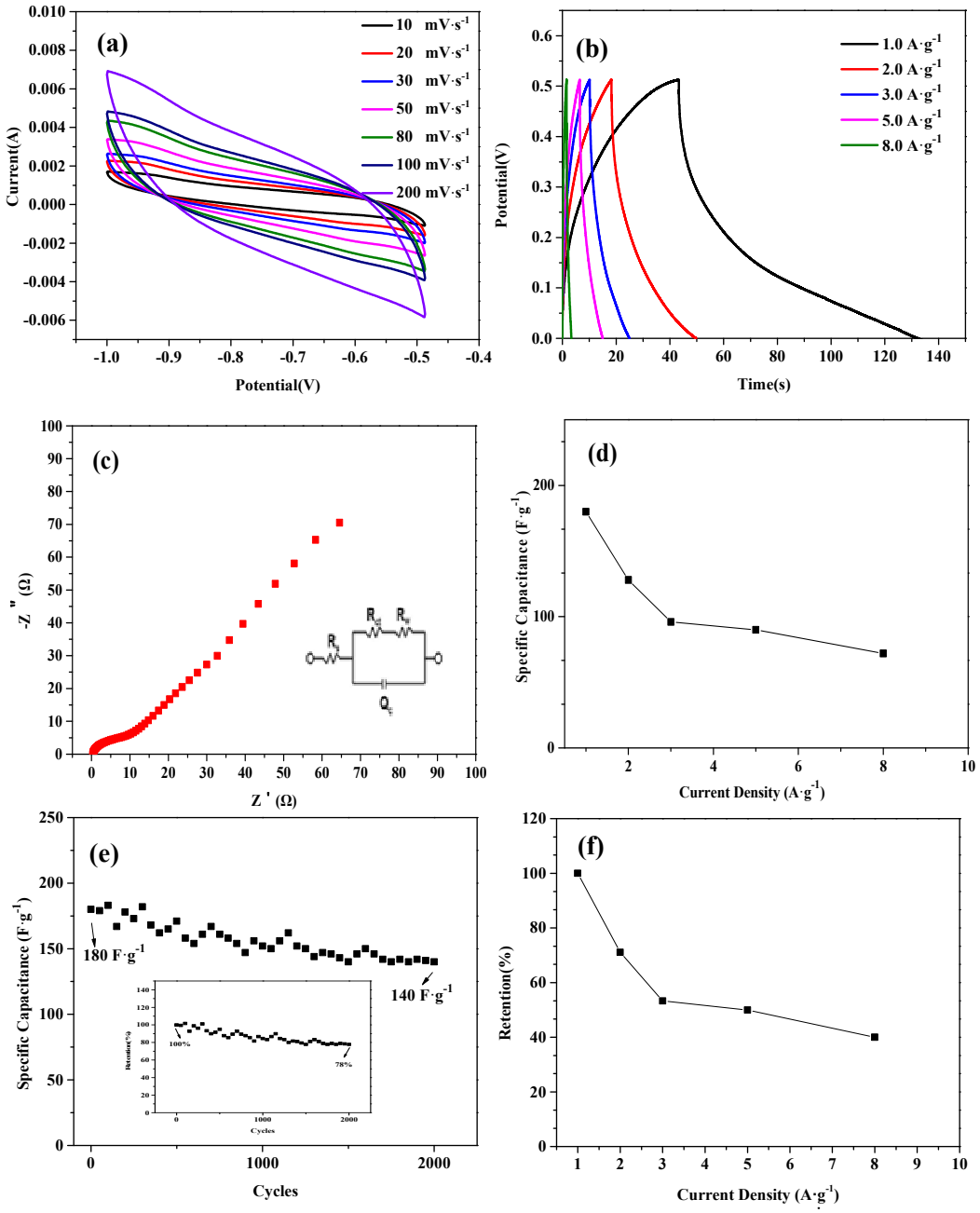

Fig. 4 Bosi Yin et al.

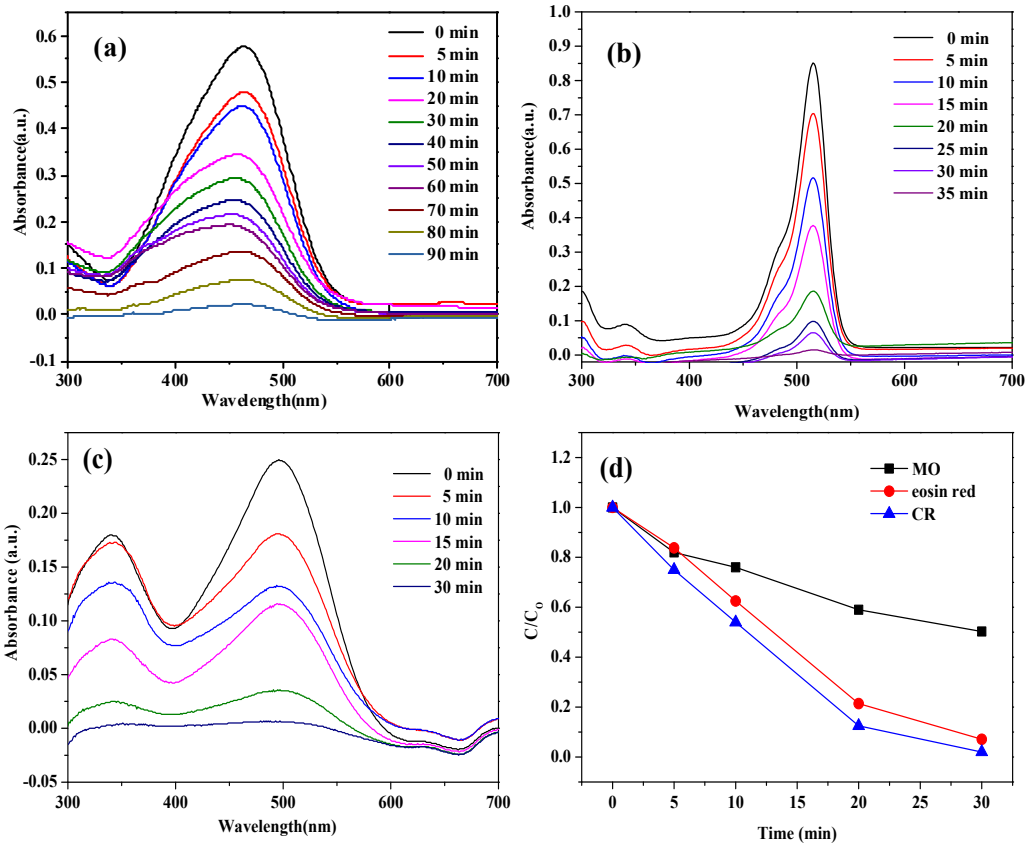

Fig. 5 Bosi Yin et al.

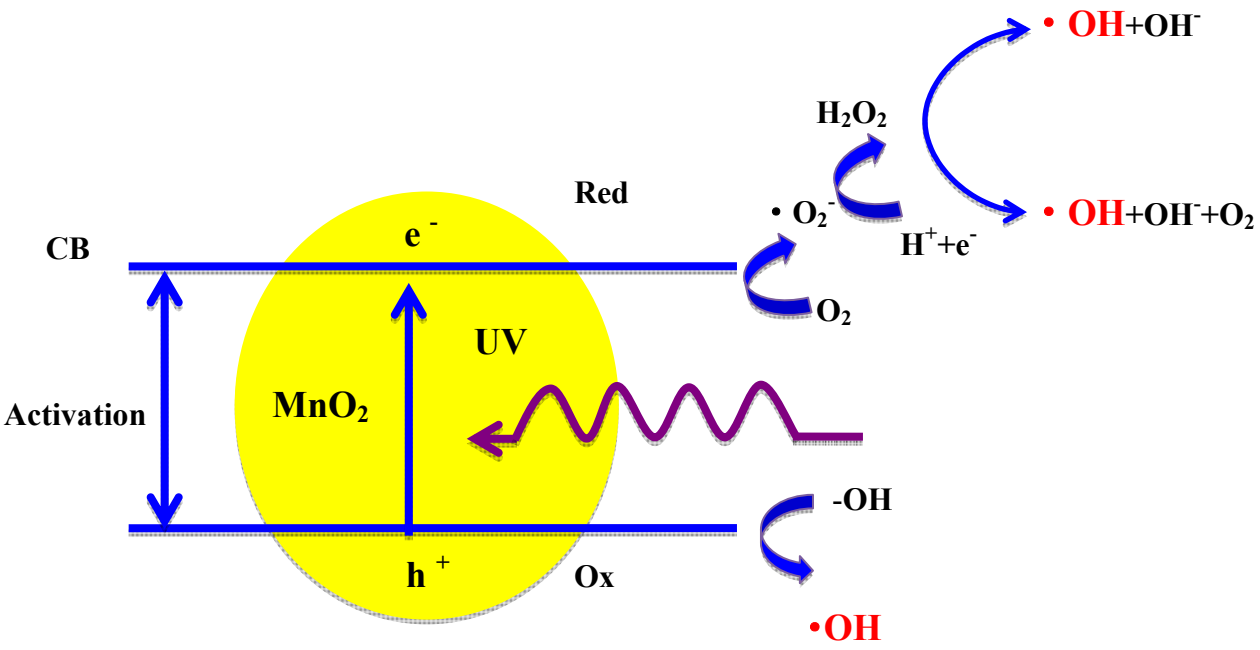

Fig. 6 Bosi Yin et al.